UNIVERSITY OF CALIFORNIA, SAN DIEGO

A Bayesian Approach to Matched-Field Geoacoustic Inversion with Analysis of ASIAEX Experimental Data

A dissertation submitted in partial satisfaction of the
requirements for the degree Doctor of Philosophy
in
Oceanography

by

Chen-Fen Huang

Committee in charge:

William S. Hodgkiss, Chair
Michael J. Buckingham
William A. Coles
Peter Gerstoft
William A. Kuperman
Robert Pinkel

2005

The dissertation of Chen-Fen Huang is approved, and it is acceptable in quality and form for publication on microfilm:

Chair

University of California, San Diego

2005

TO

MY PARENTS

FOR THEIR

UPBRINGING

AND

ENCOURAGEMENT

THROUGHOUT THE YEARS AT

SIO

TABLE OF CONTENTS

LIST OF SYMBOLS

$\mathbf{C}_{\mathrm{D}}$	Data covariance matrix
$\widehat{\mathbf{C}}_{\mathrm{M}}$	Posterior covariance matrix of model parameters
$\mathcal{CN}$	Symbol denoting the complex Gaussian distribution
$\mathbf{d}$	Vector of complex-valued pressure data; observed data
$\mathbf{d}(\mathbf{m})$	Vector for replica acoustic pressure fields (normalized to have unit length) computed from an acoustic propagation model for the model parameter $\mathbf{m}$
$\mathbf{D}(\mathbf{m})$	Forward model that maps $\mathbf{m}$ from the environmental domain to the data domain
$\mathcal{D}$	Data domain
$\boldsymbol{\eta}$	Vector of nuisance parameters
$\mathbf{I}$	Identity matrix
J	Number of processed frequencies
$\mathbf{K}$	Matrix of derivatives of the forward model with respect to a model parameter vector
$\mathcal{L}$	Likelihood function
$\mathbf{m}$	Vector of model parameters
$\widehat{\mathbf{m}}$	Maximum *a posteriori* (MAP) or maximum likelihood (ML) estimate of model parameter vector
M	Number of model parameters
M^*	Number of well-determined model parameters
$\mathcal{M}$	Environmental domain
$\mathbf{n}$	Vector of data errors; the residual variations between the observed data $\mathbf{d}$ and the modeled data $\mathbf{D}(\mathbf{m})$
N	Number of sensors in an array
ν	Variance of the data errors
$\mathrm{p}(x\|y)$	Conditional probability density function of x given y
$p(r, z)$	Acoustic pressure field at a range r and depth z
$P_{\mathrm{BT},\, l}$	Bartlett power for the l-th processed frequency
$\phi(\cdot)$	Objective function

Φ_n — n-th normal mode corresponding to the horizontal wavenumber k_{rn}

$\mathbf{R}$ — Correlation matrix of the observed data, cross-spectral density matrix

s — Complex-valued source strength

$\mathbf{u}$ — Vector of field of interest; transmission loss at different frequencies, depths and ranges

$\mathbf{U}(\mathbf{m})$ — Forward model that maps $\mathbf{m}$ from the environmental domain to the usage domain

$\mathcal{U}$ — Usage domain

LIST OF FIGURES

ACKNOWLEDGMENTS

I am gratefully indebted to Professor William Hodgkiss for suggesting this thesis problem and for guiding it to its completion. his patience, encouragement, guidance and support. I am grateful beyond words for this life changing experience.

I would like to thank Dr. Peter Gerstoft who introduces me to the world of inverse theory, which is the second subject of my dissertation. He kept my motivation high by always having his door opened to me for countless discussions on this and many other subjects.

I would like to express my gratitude to each of my committee members, Professors William Kuperman, Michael Buckingham, Robert Pinkel, and William Coles for useful comments and discussing various topics related with my study.

I would like to thank the crew of R/V *Melville*, Richard Harris, Dave Ensberg and Jeff Skinner as well as the other participants in the scientific party of ASIAEX experiment.

I would like to thank everybody in the Marine Physical Lab for their input, not only the caffeine input, or academically, but also for dragging me along on hiking or other physical activity. I wish to express my gratitude to Evelyn Doudera, Diana Stockdale, Irina Tsimring, Arron Thode, Geoff Edelmann, Seongil Kim, Katherine Kim, Karim G. Sabra, Eric Giddens, Caglar Yardim, and Rich Yen.

I would like to thank my dear friends, Fernando, Karen, Guoqing Lin, Dori, Sky Yu, and Yi-Hsien Su. From them, I have learned that there is something, other than the research, important to the life.

I would like to thank Professor Jin-Yuan Liu for introducing ocean acoustics to me during my study in National Sun Yat-sen University, 1997.

This work was supported by the Office of Naval Research, Grant Nos. N00014-01-1-0096 and N00014-01-1-0171; to them I would like to express my profound thanks for their financial support.

Finally, I wish to express my most grateful thanks to my uncle and my parents for their spiritual and financial support throughout the years at SIO. Without their understanding and support I would not have been able to give full attention to this work and to complete it successfully.

The text of Chapter Two in part is a reprint of the material as it appears in Chen-Fen Huang and William S. Hodgkiss, "Matched field geoacoustic inversion of low frequency source tow data from the ASIAEX East China Sea experiment," IEEE J. Oceanic Eng., Vol. 29, 952–963, 2004. The dissertation author was the primary researcher/author and the co-author listed in this publication directed and supervised the research which forms the basis for this chapter.

VITA

1995	B.S., National Sun Yat-sen University, Kaohsiung, Taiwan
1997	M.S., National Sun Yat-sen University, Kaohsiung, Taiwan
1998	M.S., National Sun Yat-sen University, Kaohsiung, Taiwan
1998–2000	Research Assistant, National Sun Yat-sen University, Kaohsiung, Taiwan
2005	Doctor of Philosophy University of California, San Diego

PUBLICATIONS

Journals

1. Chen-Fen Huang, Peter Gerstoft, and William S. Hodgkiss, "Uncertainty analysis in matched-field geoacoustic inversion," J. Acoust. Soc. Am., (accepted upon revision, 2005)
2. Peter Gerstoft, Chen-Fen Huang, and William S. Hodgkiss, "Estimation of transmission loss in the presence of geoacoustic inversion uncertainty," IEEE J. Oceanic Eng., (in press, 2005)
3. Chen-Fen Huang and William S. Hodgkiss, "Matched field geoacoustic inversion of low frequency source tow data from the ASIAEX East China Sea experiment," IEEE J. Oceanic Eng., Vol. 29, 952–963, 2004.
4. Jin-Yuan Liu, Ping-Chang Hsueh, and Chen-Fen Huang, "Coherent reflection of acoustic plane wave from a rough seabed with random sediment layer overlying an elastic basement," IEEE J. Oceanic Eng., Vol. 27, 853–861, 2002.
5. Jin-Yuan Liu, Chen-Fen Huang, and Ping-Chang Hsueh, "Acoustic plane-wave scattering from a rough surface over a random fluid medium," Ocean Engineering, Vol. 29, No. 8, 915–930, 2002.
6. Bang-Fuh Chen and Chen-Fen Huang, "Hydrodynamic forces on concrete sea wall and breakwater during earthquake: effects of bottom sediment layers and back-fill soil," Ocean Engineering, Vol. 29, No. 7, 783–814, 2002.
7. Jin-Yuan Liu, Chen-Fen Huang, and Shiahn-Wern Shyue, "Effects of seabed properties on acoustic wave fields in a seismo-acoustic ocean waveguide," Ocean Engineering, Vol. 28, No. 11, 1437–1459, 2001.
8. Jin-Yuan Liu and Chen-Fen Huang, "Acoustic plane-wave interaction with a randomly inhomogeneous slab bounded by rough surfaces," Journal of Sound and Vibration, Vol. 241(3), 441–457, 2001.
9. Jin-Yuan Liu and Chen-Fen Huang, "Acoustic plane-wave reflection from a rough surface over a random fluid half-space," Ocean Engineering, Vol. 28, No. 7, 751–762, 2001.

10. Jin-Yuan Liu and Chen-Fen Huang, “Acoustic plane-wave scattering from a rough interface over an inhomogeneous transition fluid layer,” Ocean Engineering, Vol. 28, No. 6, 603–619, 2001.
11. Jin-Yuan Liu and Chen-Fen Huang, “Effects of medium inhomogenieties on surface-generated ambient noise,” Proc. Natl. Sci. Counc. ROC(A), Vol. 25, No. 1, 45–52, 2001.
12. Jin-Yuan Liu, Chau-Chang Wang, and Chen-Fen Huang, “Coherent reflection from a rough interface over an inhomogeneous transition fluid layer,” Journal of Computational Acoustics, Vol. 8, No. 3, 401–414, 2000.
13. Jin-Yuan Liu and Chen-Fen Huang, “Surface-generated noise in an ocean waveguide with a transition layer of continuously varying density and sound speed,” Journal of Computational Acoustics, Vol. 7, No.4, 253–268, 1999.
14. Bang-Fuh Chen and Chen-Fen Huang, “Nonlinear hydrodynamic pressures generated by a moving high rise offshore cylinder,” Journal of Ocean Engineering, Vol. 24, No. 3, 201–216, 1997.

Conference Proceedings

1. Caglar Yardim, Peter Gerstoft, William S. Hodgkiss, and Chen-Fen Huang, “Refractivity from clutter (RFC) estimation using a hybrid genetic algorithm – Markov chain Monte Carlo method,” IEEE APS international and USNC/URSI National Radio Science meeting, 2005.
2. Peter Gerstoft, Chen-Fen Huang, and William S. Hodgkiss, “Estimation of transmission loss and its uncertainty,” Conference on Acoustic Inversion methods and Experiments, Ischia, 2004.
3. Peter Gerstoft, Chen-Fen Huang, William S. Hodgkiss, and Peter Nielsen, “Posterior transmission loss from ocean acoustic data,” Sixth European conference on underwater acoustics, Delft, 2004.
4. Chen-Fen Huang and William S. Hodgkiss, “Mid-frequency geoacoustic inversion of source tow data from the ASIAEX East China Sea experiment,” Oceans2003 MTS/IEEE Conference Proceedings, San Diego, California, 576–581, 2003.
5. Jin-Yuan Liu and Chen-Fen Huang, “Surface-generated noise in an ocean waveguide with an inhomogeneous transition layer,” Oceans’99 MTS/IEEE Conference Proceedings, Seattle, Washington, Vol. 1, 439–445, 1999.

Presentations with Abstract

1. Jin-Yuan Liu, Li Ding, and Chen-Fen Huang, “The Concept of acoustic monitoring in Kaohsiung harbor area in Southern Taiwan,” Turkish International Conference on Acoustics, Istanbul, Turkey, 2005.
2. Chen-Fen Huang, Peter Gerstoft, and William S. Hodgkiss, “Influence of data uncertainty on matched-field geoacoustic inversion,” J. Acoust. Soc. Am., 115, 2409, 2004.
3. Peter Gerstoft, Chen-Fen Huang, and William S. Hodgkiss, “Iterative geoacoustic inversion,” J. Acoust. Soc. Am., 115, 2408, 2004.
4. Chen-Fen Huang and William S. Hodgkiss, “Geoacoustic inversion results of low- to high-frequency source tow data from the ASIAEX East China experi-

ment," J. Acoust. Soc. Am., 114, 2344, 2003.

5. Chen-Fen Huang and William S. Hodgkiss, "Source tow geoacoustic inversions from the 2001 ASIAEX East China Sea experiment," J. Acoust. Soc. Am., 112, 2283, 2002.
6. Chen-Fen Huang, Philippe Roux, and William A. Kuperman, "Computing the two-point correlation function directly from the transport equation using split-step Padé solutions," J. Acoust. Soc. Am., 112, 2394, 2002.
7. Chen-Fen Huang and William S. Hodgkiss, "Low-frequency source tow geoacoustic inversions from the 2001 ASIAEX East China Sea experiment," J. Acoust. Soc. Am., 112, 2283, 2002.

FIELDS OF STUDY

Major Field: Applied Ocean Science

Studies in Applied Mathematics.
Professors William R. Young and Stefan L. Smith

Studies in Physical Oceanography.
Professors Lynne D. Talley and Myrl C. Hendershott

Studies in Biological Oceanography.
Professors Lisa Ann Levin and David Checkley

Studies in Marine Chemistry.
Professors Joris M. Gieskes and Ralph F. Keeling

Studies in Marine Geology.
Professor Peter F. Lonsdale

Studies in Underwater Acoustics.
Professors William A. Kuperman and Michael J. Buckingham

Studies in Digital Signal Processing and Array Signal Processing.
Professor William S. Hodgkiss

Studies in Geophysical Inverse Theory.
Professor Catherine G. Constable

ABSTRACT OF THE DISSERTATION

A Bayesian Approach to Matched-Field Geoacoustic Inversion
with Analysis of ASIAEX Experimental Data

by

Chen-Fen Huang
Doctor of Philosophy in Oceanography
University of California, San Diego, 2005
Professor William S. Hodgkiss, Chair

This dissertation applies a Bayesian framework for making quantitative statistical inferences about geoacoustic properties from ocean acoustic data using matched-field processing techniques. Data acquired during the ASIAEX 2001 East China Sea experiment are used to infer the geoacoustic properties.

In a Bayesian approach, information and uncertainty regarding model parameters obtained from the measurements are summarized in the posterior probability distribution. This posterior distribution is proportional to the product of a prior distribution (which incorporates information on model parameters before the measurements) and of a likelihood function (which quantifies how well a model fits the measurements). From this posterior distribution of model parameters, we obtain all information about the model parameters, such as maximum *a posteriori* estimate (best-fit model), mean as well as standard deviation.

The quality of the best-fit model is checked using matched-field processing for source localization. In the less than 1 kHz frequency band, the effect of environmental mismatch on source tracking can be reduced by using inversion techniques to estimate geoacoustic parameters, resulting in improved source localization performance. The parameter uncertainty (in terms of mean and standard deviation) given by the Bayesian approach is validated by comparing the variabilities of the estimated parameters inverted from multiple independent data sets.

A Bayesian approach to inverse problems requires estimation of the uncertainties in the data. An extension of the Bayesian parameter uncertainty analysis to include the uncertainty of data errors is carried out. Following a full Bayesian methodology, we derive the analytic expressions for the posterior probability distribution of the model parameters for both single and multi-frequency data.

The impact of uncertainty embedded in the geoacoustic inversion results on the estimation of transmission loss is investigated. An approach for estimating the statistical properties of transmission loss is developed using information on the model parameters obtained from the inversion. The utility of this approach is that one can compute the probability distributions of transmission loss at all frequencies, ranges and depths. Examples demonstrate the use of transmission loss probability density functions to extract characteristic features such as median and lower/upper percentiles.

Chapter 1

Introduction

1.1 Background and Objectives

Inferring geoacoustic properties indirectly from the measured sound fields in an oceanic environment using various signal processing schemes, referred to as ocean geoacoustic inversion, is an important application of underwater sound. This subject has attracted the attention of several researchers in the past decade, resulting in both theoretical [10,21,22,24,27–35,38,39,41] and experimental [13,25,29,40,42,57,75] work. Many studies have shown that even though the inversion results may present some degree of uncertainty, the techniques still prove to be a valuable and promising means of estimating environmental parameters. In particular, geoacoustic inversion is most useful for estimating those environmental variables that are difficult to approach directly on site, such as the density and sound speed (compressional or shear) profiles of the sea floor.

The primary objective of this dissertation is to carry out an analysis of geoacoustic inversion, based upon field data obtained in the Asian Seas International Acoustics EXperiment (ASIAEX). ASIAEX was an international scientific endeavor involving ocean acousticians from the United States and several countries surrounding the west Pacific Rim, including the People's Republic of China, the Republic of Korea, Japan, Taiwan, Russia, and Singapore. The major field experiments of ASIAEX were conducted from May to August of 2001 and consisted of two parts: the South China Sea (SCS) experiment and the East China Sea (ECS) experiment. The SCS experiment placed emphases on acoustic propagation over the continental shelf and acoustic interactions with a dynamic oceanographic environment (specifically, internal waves), while the ECS experiment concentrated on boundary interactions, reverberation, and geoacoustic inversion. The complete program and some results to-date have been published in the IEEE Journal of Oceanic Engineering Special Issue on the Asian Marginal Seas (2004) [59].

As a part of the ASIAEX ECS program, data were collected to invert for the geoacoustic properties in the ECS using acoustic measurements over the frequency range of $O(100 - 1000)$ Hz. The data obtained are analyzed in this thesis. These data supplemented by the comprehensive oceanographic and geophysical measurements also obtained during the experiment are used to assess quantitatively the reliability of the inverted parameters and the employed seafloor model.

During the past decade, substantial effort has been devoted to the development of computational algorithms for inversion [27–29, 32, 33]. Among others, the SAGA program for geoacoustic inversion [34] has been widely accepted and is used in this research. The state-of-the-art has reached the point that many important issues such as uncertainties due to measurement noise and modeling errors as well as robustness for *a posteriori* estimation are now worthy of more consideration. These subjects also constitute another part of the objectives of this dissertation.

1.2 Basic Concepts

Matched-Field Geoacoustic Inversion

In this thesis, matched-field (MF) geoacoustic inversion techniques are applied to estimate seafloor properties. The concept of MF processing where a passive array of receivers is used to locate in range and depth (and bearing) an acoustic source traveling in a *known* oceanic environment was introduced to the underwater acoustics community by Bucker [10]. Many studies [10, 21, 30, 39, 41] have shown that MF processing for source localization is sensitive with respect to the variations of, or the "mismatch" of, the environmental parameters, such as sound speed profiles, water depth, seabed properties, etc. As a result, the concept of employing the procedure "inversely" by treating the environment, and/or source position itself, as *unknowns* and obtaining them from the

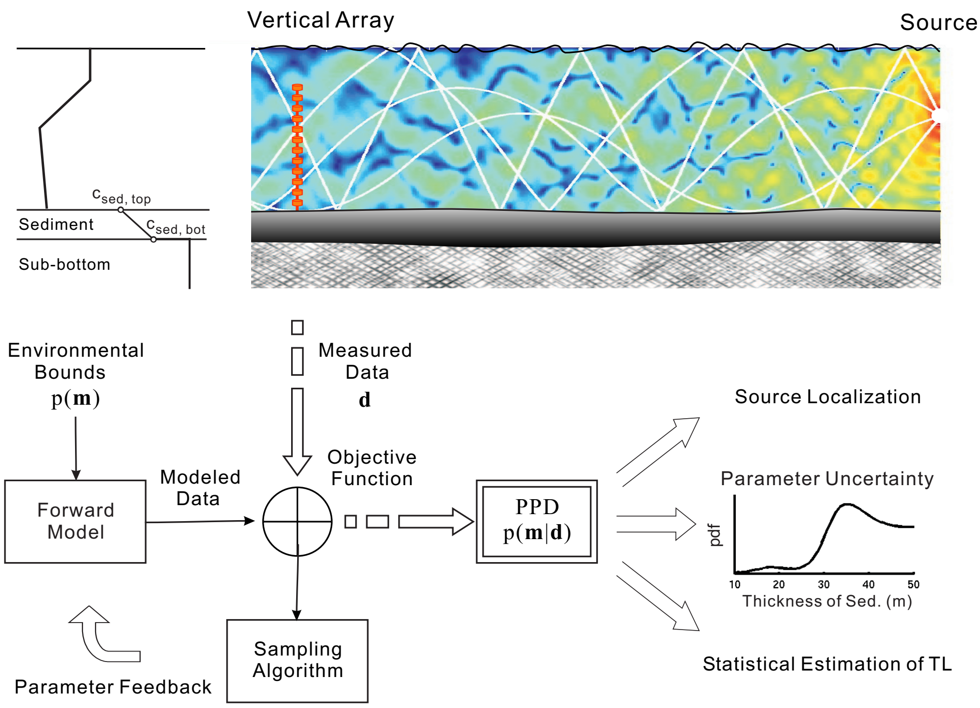

Figure 1.1: Bayesian approach to matched-field geoacoustic inversion.

sound field has been conceived and developed [25, 31, 40, 42].

MF geoacoustic inversion uses measurements of the acoustic field made at an array of hydrophones to extract information on the parameters that determine sound propagation in the ocean. The procedure is shown schematically in Figure 1.1. Given some measured data and some prior information on the values of a parameterized environmental model (e.g., the ocean and sediment sound speeds, attenuations and their thicknesses), a theoretical relationship (the forward model) is constructed to relate the predicted data to the environmental model parameters. Then, by minimizing an appropriate objective function that measures the difference between the measured data and the predictions from the forward model, a set of parameters that best describes the environment is obtained.

Due to the fact that inversion problems make inferences about the environmental parameters using a finite set of noisy data, one always faces the problem of nonuniqueness, i.e., more than one solution can represent the data at hand. The Bayesian approach is adopted in this analysis. The solution of the inverse problem is not only to find a single model parameter vector that fits the measurements best, referred to as the best-fit model, but also to assess the uncertainty of the estimated model parameter.

Bayesian Approach

Since the analysis of geoacoustic inversion always involves errors (noise) and uncertainties in the observed data and model parameters, which may be characterized by probability density functions, probability theory is thus invoked in this study.

There are, however, two different interpretations of probability [76, p. 16][60, p. 25]. In the "frequentist" interpretation, probability is used to describe the likelihood of a particular event occurring in a series of repeated experiments; the higher the value, the more it is likely to occur. On the other hand, in the "Bayesian" interpretation [50], probability is simply used to describe the degree of belief of a predicted value, based upon a single experiment. Here, the Bayesian framework of probability is adopted.

The probabilistic approach in geophysics was pioneered by Tarantola and Valette [78], and Tarantola [76]. The formulation presented in the Tarantola's book is general enough to cover a wide variety of problems in applications. Recently, the Bayesian framework has been adopted in underwater acoustics by some researchers [22, 32, 38].

The fundamental objective of Bayesian inference is to obtain the posterior probability distribution (PPD) of the model parameters. This posterior distribution consists of the product of two probability density functions. The first, the likelihood function, defines what it means for a model to fit the data. The likelihood function quantifies the misfit between the measured data and the modeled data generated by a forward model. Thus, this function takes into account the noise in the measured data as well as the error in the forward modeling procedure. The second, the prior density function, incorporates our *a priori* understanding of model parameters before having access to the measured data.

Using a Bayesian approach to inverse problems requires estimation of the uncertainties in the data due to ambient noise as well as modeling errors. The variance parameter of the Gaussian error model, referred to as error variance, is assumed to describe the data uncertainties. In practice, this parameter is often poorly known *a priori*, and choosing a particular value is often problematic. Hence, to account for the uncertainty in the error variance, several methods are introduced to implement both the full and the empirical Bayesian approaches. A full Bayesian approach permitting uncertainty of the error variance to propagate through the parameter estimation processes is a natural approach. However, the computational effort is substantial. Thus, several methods using an empirical Bayesian approach were developed in which the posterior distributions of model parameters are conditioned on a point estimate of the error variance.

Using the Inversion Results: *A Posteriori* Analysis

In Bayesian inference, all information on the model parameters is derived from the PPD. Such information can be expressed in many ways, for instance, as error bars on the parameter estimates, or marginal PPDs of the model parameters. All of these are explored in this work.

The variability in the geophysical properties of the ocean bottom has a significant impact on sonar performance in shallow water. A key element in the sonar equation is transmission loss (TL) which requires the information on the geoacoustic properties at site.

Recent work related to translating the environmental uncertainty to sonar performance predictions has been undertaken by Abbot and Dyer [1]. In their approach, a probabilistic description of TL was estimated at a given range where many acoustic measurements were made. Then the TL probability density function is assumed to apply universally for all ranges. It does not account for the spatial variations of TL due to multi-path propagation.

Here, we use a Bayesian probabilistic approach to estimate the statistical properties of TL in the presence of geoacoustic inversion uncertainty. Since TL is estimated from a full wave solution, the resulting probability density function of TL should be more representative.

1.3 Scope of the Dissertation

The major contents of this dissertation consist of four chapters, Chapters 2 to 5[1]. Chapter 2 is devoted to the analysis of ASIAEX ECS experimental data. The

[1]Each chapter has been written in a paper format. As of this date, they either have been accepted for publications or published in a professional journal or conference proceeding.

experimental geometry, acoustic, oceanographic, and seismic measurements are first described and analyzed. A parameterized environmental model is proposed to describe the experimental region. Then the inversion procedure based on MF processing using low-frequency data (195, 295, and 395 Hz) is applied to estimate the model parameters. The quality of the inversion results are gauged by two different approaches. First, the best-fit model is confirmed by continuous source localization over a period of time. Second, a comparison of the uncertainties of the parameter estimation provided by the Bayesian procedure with those obtained by separate inversions at many different ranges (a frequentist approach) is made and analyzed [46].

In Chapter 3, the analysis is extended from low-frequency to include mid-frequency data (805, 850, and 905 Hz) in the inversion procedure. First, a test run of mid-frequency MF source localization is carried out using the best-fit model derived from lower frequency data. Motivated by the increased ambiguity in the estimated source position, a refined estimate of the environmental model is obtained by incorporating the mid-frequency data in the inversion. The quality of the refined model is again confirmed by continuous source localization over the same period of time as in the low frequency data case [45].

Chapter 4 addresses the issue of uncertainty estimation using the Bayesian statistical treatment. The uncertainty of each estimated parameter is quantified by the variance associated with it, and analysis is then carried out by several methods based upon both the full and the empirical Bayesian approaches [44].

In Chapter 5, *a posteriori* analysis is undertaken using the inverse solution as an intermediate step to estimate TL. TL is estimated by first solving for an ensemble of relevant environmental model parameters and then using this ensemble to map into the TL domain. The probability distribution of TL is presented along with its statistical properties such as median and lower/upper percentiles [37].

Finally, Chapter 6 addresses the conclusions of the thesis and suggestions for future research.

Chapter 2

Geoacoustic Inversion of Low-Frequency Data

Geoacoustic inversion results based on data obtained during the Asian Seas International Acoustics Experiment (ASIAEX) 2001 East China Sea experiment are presented. The inversion process uses a genetic-algorithm-based matched-field-processing approach to optimize the search procedure for the unknown parameters. Inversion results include both geometric and geoacoustic variables. To gauge the quality of the inversion, two different analyses are employed. First, the inversion results based upon discrete source-receiver ranges are confirmed by continuous source localization over an interval of time. Secondly, separate inversions at many different ranges are carried out and the uncertainties of the parameter estimation are analyzed. The analysis shows that both methods yield consistent results, ensuring the reliability of inversion in this study.[‡]

2.1 Introduction

Probing geoacoustic properties indirectly from acoustic sound fields in an oceanic environment is an important application of underwater sound and has attracted the attention of several authors in recent years [35, 40, 42, 75]. Many studies have shown that even though the inversion results may present some degree of uncertainty, the techniques

[‡]The contents of this chapter are adapted from the paper entitled "Matched field geoacoustic inversion of low frequency source tow data from the ASIAEX East China Sea experiment" by Chen-Fen Huang and William S. Hodgkiss, *IEEE Journal of Oceanic Engineering*, Vol. 29, 952–963, 2004.

still prove to be an efficient and promising way to estimate environmental variables, particularly for those that are difficult to measure directly on site.

The purpose of this chapter is to present the geoacoustic inversion results based upon source tow data obtained during the Asian Seas International Acoustics Experiment (ASIAEX) 2001 East China Sea experiment. The experimental site, as depicted in the upper panel of Fig. 2.1, is in the East China Sea, and is located roughly at 500 km off the coast of the Zhejiang Province in east China. The thick curve in the figure illustrates the ship track of R/V *Melville* from Julian day (JD) 149 to 162 of 2001.

During the experiment, both acoustic and oceanographic data were collected. These data are analyzed to invert for the geoacoustic properties of the waveguide. In this analysis, matched-field (MF) inversion techniques are applied to estimate the environmental parameters. The basic principle of the MF inversion technique is to estimate the unknown parameters by minimizing an objective function that quantifies the mismatch between measured acoustic fields and simulated replica fields derived from an acoustic propagation model in a parameterized environment. The best estimates for the unknown parameters then correspond to the lowest mismatch. Since the dimension of the search space depends upon the number of unknown parameters which sometimes may be large, an efficient algorithm is needed to optimize the global search procedure. In this regard, a few methods geared to global optimization, such as simulated annealing and genetic algorithms, have been developed [18, 19, 25, 27, 32]. Furthermore, in the past decade, several authors, e.g., [34, 73, 80], have implemented inversion procedures in terms of computational software. Among others, the genetic-algorithm-based software SAGA developed by Gerstoft [34] has been widely applied and is used in this analysis along with the normal-mode propagation model SNAP [52] for a range-independent environment.

To ensure the robustness of the inversion, two different analyses were employed and both have yielded consistent results. The chapter is organized as follows: Sections 2.2 and 2.3 provide, respectively, the descriptions of the data acquisition and the data processing. Section 2.4 outlines the MF inversion procedure, and Section 2.5 presents the inversion results, followed by a conclusion in Section 2.6.

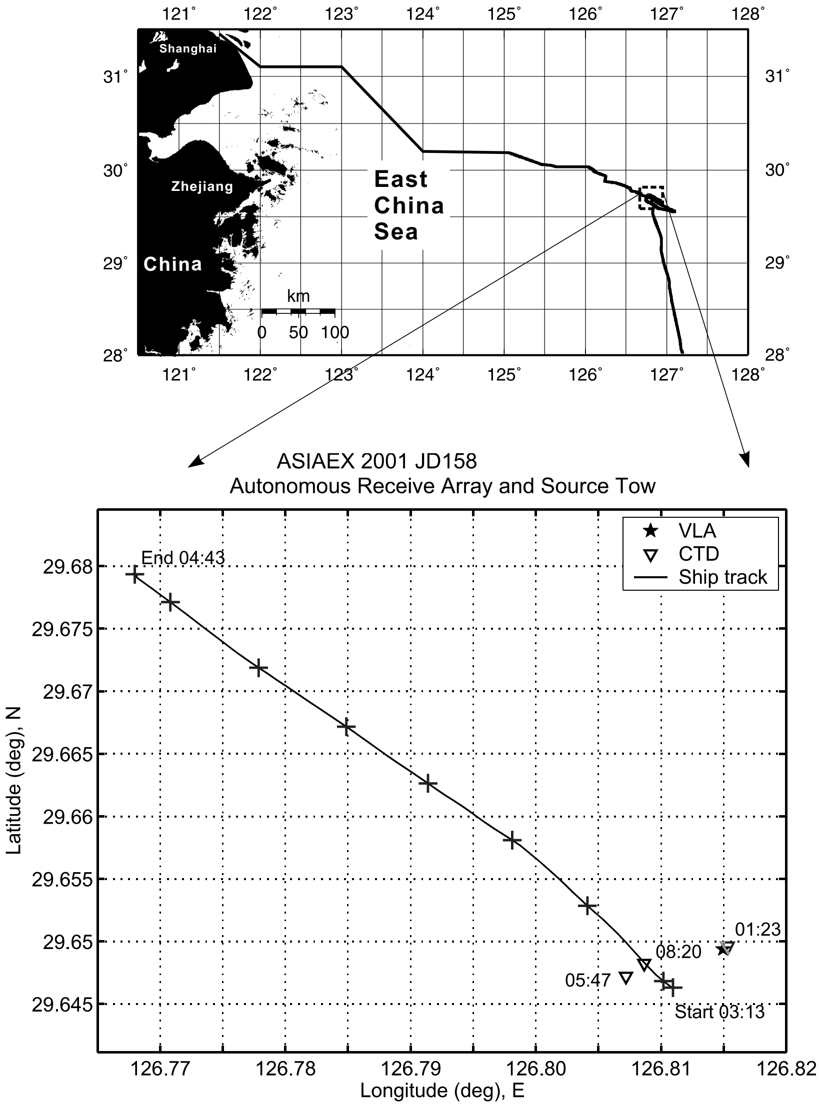

Figure 2.1: Plan view of the ASIAEX 2001 East China Sea experiment. Upper panel: the thick line illustrates the track of R/V *Melville* during the Julian days (JD) 149 – 162. Lower panel: the line is the ship track where the source energy was transmitted, and the plus signs mark 10-minute intervals starting from the acoustic measurement. The triangle signs represent the locations where the CTD measurements were taken. The star sign indicates the location of the vertical line array (VLA). All times are in Coordinated Universal Time (UTC).

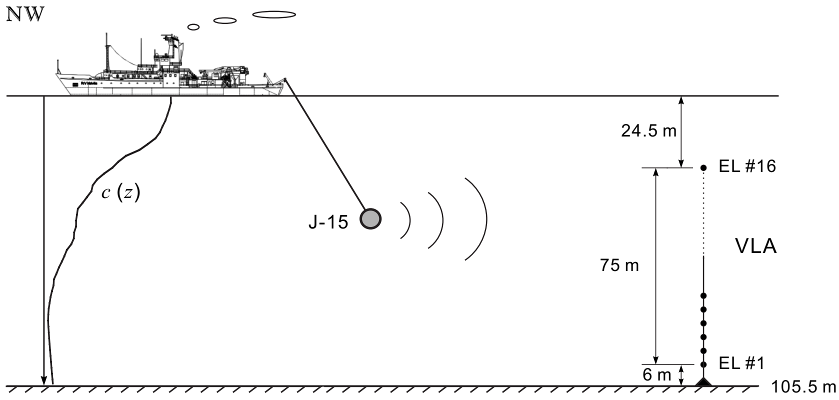

Figure 2.2: Side view of the experimental geometry.

2.2 Data Acquisition

In the following subsections, a few details of the experiment as well as the characteristics of the acquired data are described. These include experimental geometry, oceanographic and seismic measurements.

2.2.1 Experimental Geometry

The map of the region where the acoustic and oceanographic measurements were taken is shown in the lower panel of Fig. 2.1. On JD 158, acoustic energy was transmitted from the J-15 source towed near 47 m depth by R/V *Melville* with a speed of about 3 knots. The ship track is indicated by the line in the figure, on which the distances between the source and the receiver range from 0.5 to 6 km. The experimental geometry is illustrated schematically in Fig. 2.2. A 16-element, 75-m aperture, autonomous recording vertical line array (VLA) was moored up from the seafloor at location 29°38.927′ N, 126°48.892′ E where the measured water depth was approximately 105.5 m. The lowermost element (element #1) was approximately 6 m above the bottom; Element #4 failed during deployment.

Continuous-wave (CW) tonals at 95, 195, 295, 395, 805, 850, and 905 Hz were transmitted and the sound field was recorded from 0313 to 0443 Coordinated Universal Time (UTC). In this study, only the low frequency data at 95, 195, 295, and 395 Hz are employed for inversion analysis.

2.2.2 Oceanographic Measurements

The current profile in the water column from 30 to 100 m was measured by a ship-mounted ADCP system on board R/V *Melville*. The ADCP measurement from JD 158 to 158.25 is shown in Fig. 2.3. The upper and lower panels illustrate, respectively, time-series plots of current speed and current vector stick at different depths. The time window of the acoustic transmissions is indicated by the two white lines on the upper panel and the shaded area on the bottom. It is noted that there existed a strong eastward tidal current with magnitude greater than 0.5 m/s around the middle of the water column. This results in a tilt of the VLA.

The sound-speed profile in the water column was measured by CTD. Three measured sound-speed profiles on JD 158 are shown in Fig. 2.4, on which the times when the measurements were taken are labeled. CTD0123 (solid line) was the profile when the VLA was deployed; CTD0547 (dashed line) and CTD0820 (dashed-dotted line) were the profiles measured roughly 1 and 4 hours after the acoustic tonals were transmitted, respectively.

The locations of CTD measurements are indicated in the lower panel of Fig. 2.1. These sound-speed profiles show that higher sound speed near the surface and, in the thermocline layer, time-evolving sound speed fluctuations were observed, while below 75 m the sound speed remained the same. Note that for a sound source at about 47 m as in the present case, the sound speed structure will result in a downward-refracting propagation pattern, so that strong interactions of the sound fields with the seafloor might be expected.

2.2.3 Seismic Measurements

Geoacoustic ground truth measurements of the region covered by $28^\circ - 30^\circ$N and $126^\circ 30' - 128^\circ$E were made in 2000 and 2001 as part of the ASIAEX East China Sea field program. The surveys include gravity and piston cores and water-gun and chirp sonar generated subbottom profiles. The detailed discussion on geoacoustic measurements are presented in Miller *et al.* [67]. In short, these data suggest that the sedimentary bottom presents a layered structure. The thickness of the upper layer from seafloor to Transgressive Systems Tract (TST) is about 0 to 2 m, and that of the lower

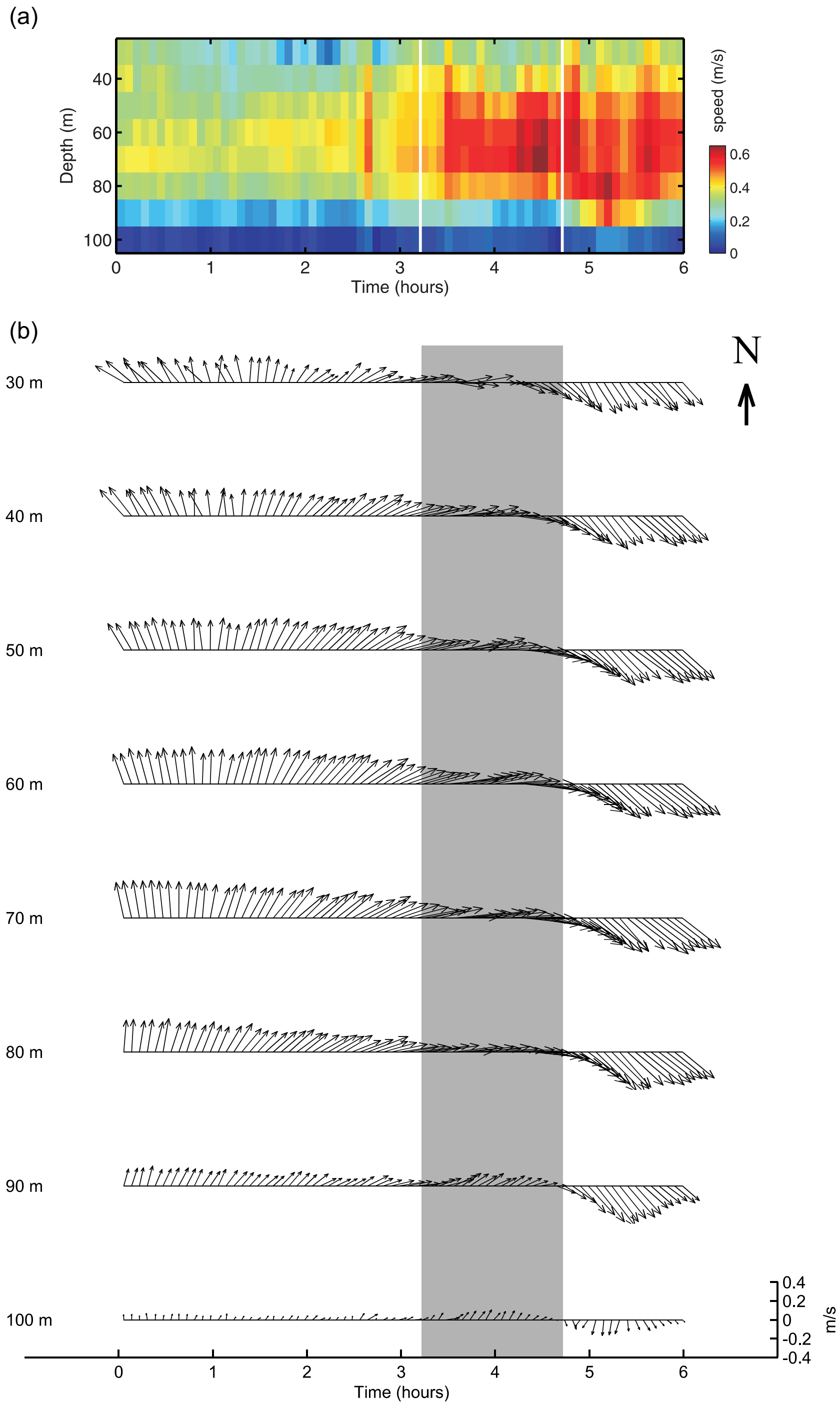

Figure 2.3: Time-series plots of current speed (upper panel) and current vector stick (bottom panel) at different depths from JD 158 to 158.25. The time windows of the acoustic transmissions are indicated by the two white lines on the upper panel and the shaded area on the bottom.

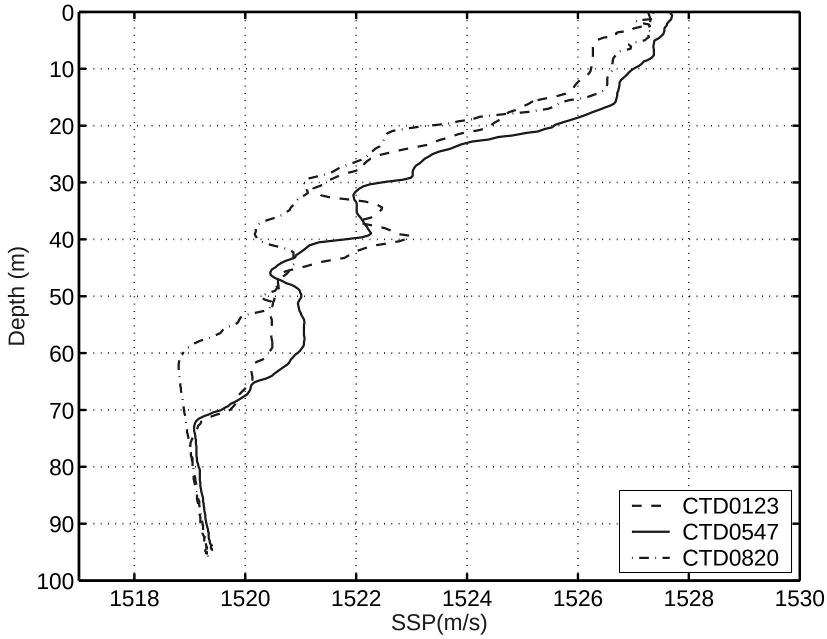

Figure 2.4: Measured sound-speed profiles by the CTDs on JD 158. Each sound-speed profile is labeled by the time when the measurement was taken. The locations of the CTD measurements are indicated in Fig. 2.1.

layer from TST to Sequence Boundary (SB) is about 5 to 7 m at the site of towed source propagation experiments. Moreover, the sediment coring analysis indicates this region spanned a surficial sediment "front" consisting of mud-and-sand type of sediment to the west and sand to the east. The acoustic experimental site was located to the west of the front; a mean grain size (in phi scale) of 4.3 ϕ consistent with mud-and-sand-like sediment. The coring data also show a sound speed going from approximately 1575 m/s at the water-sediment interface to 1600–1675 m/s at approximately 1 m into the sediment.

2.3 Data Processing

The entire 90-minute time series data were processed using 262,144-point FFTs with 50% overlap. With a sampling rate of 20470.8 samples/sec (the bin width is 0.0781 Hz), the time duration of each FFT (snapshot) is 12.805 sec and the interval between consecutive snapshots is 6.40 sec. The long length of the snapshot is to ensure high signal-to-noise ratio (SNR). Due to the narrow bin width and the Doppler shift resulting from ship motion, the frequency bin selected for the inversion needs to be chosen with care. For each snapshot and frequency, the bin chosen corresponds to the bin containing the highest average power across the array. Since there are 15 functioning array elements, there are 15 complex pressure values sampling the acoustic field across the water column for each snapshot. Figure 2.5 shows the calibrated time-evolving signal power across the array for 95, 195, 295, and 395 Hz, and the corresponding noise floor which is estimated by averaging over the 15 adjacent bins separated from the signal bin by 5 bins. In this figure, the vertical axis is the element number with element #1 being the deepest transducer. Note that at 95 Hz the SNR is very low and this frequency is not used in the inversion. In contrast, the SNR is high for the frequencies 195, 295, and 395 Hz.

The estimated normalized cross-spectral density matrix (CSDM), $\widehat{\mathbf{R}}$, for a signal frequency is given by

$$\widehat{\mathbf{R}} = \frac{\langle \mathbf{d}\mathbf{d}^{\dagger} \rangle}{\mathrm{Tr}\left[\langle \mathbf{d}\mathbf{d}^{\dagger} \rangle\right]}, \tag{2.1}$$

where $\mathbf{d}$ is the vector containing the measured complex pressures, and $\langle\cdot\rangle$ and $\dagger$ denote, respectively, the average over several snapshots and the complex transpose operation. The covariance matrix is normalized by its trace. The maximum obtainable Bartlett

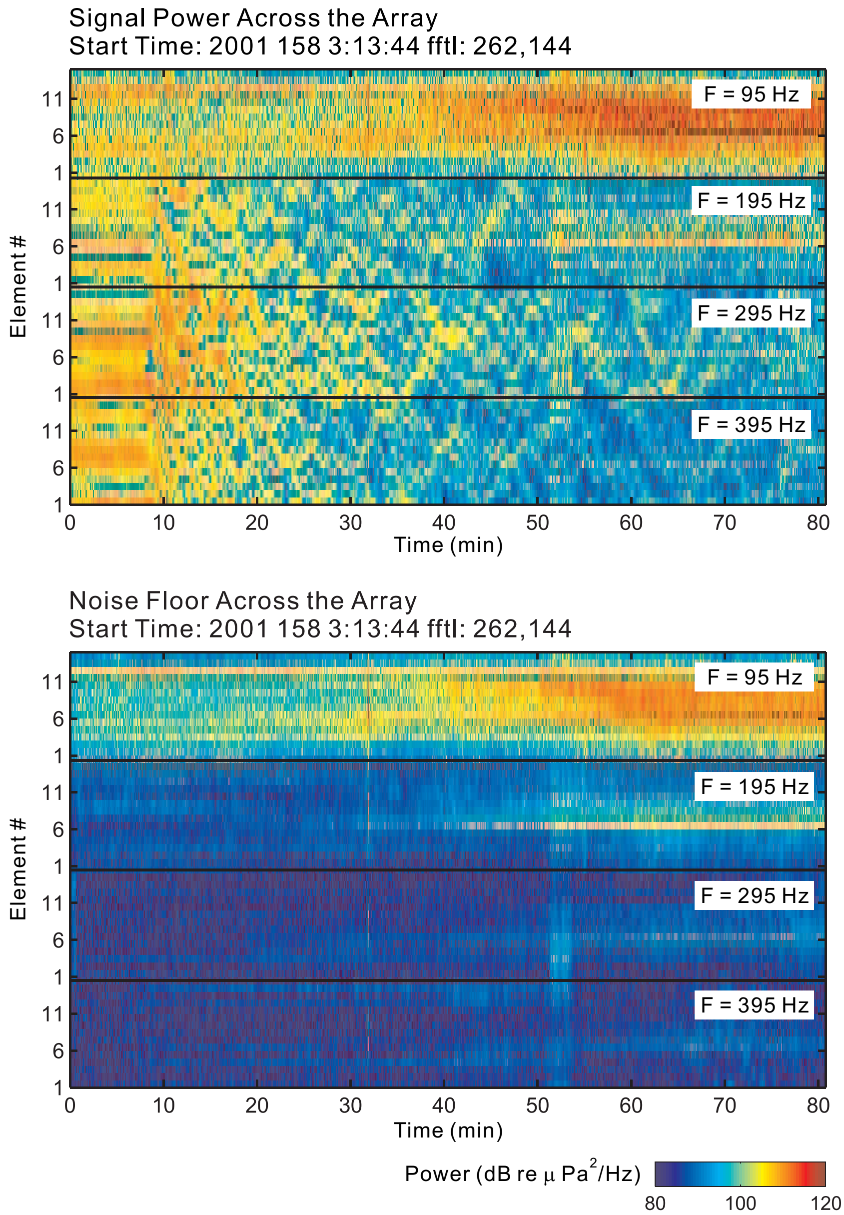

Figure 2.5: Time-evolving signal power (upper panel) and noise floor (lower panel) across the elements for 95, 195, 295, and 395 Hz.

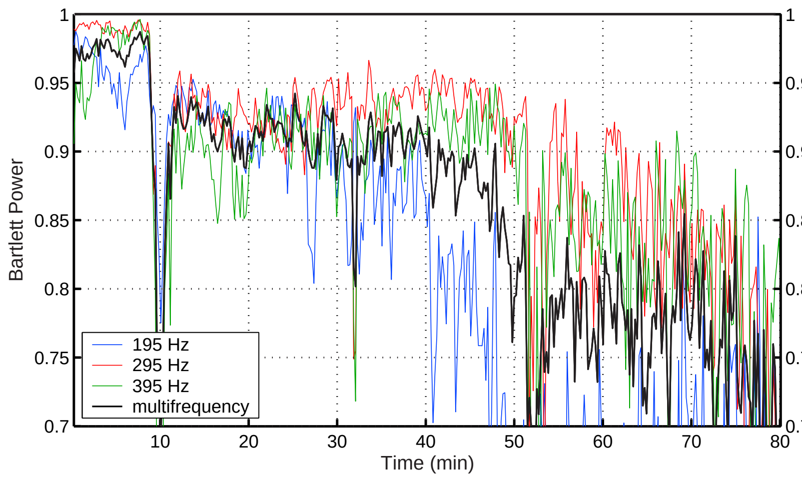

Figure 2.6: Maximum obtainable Bartlett power versus time: the thin lines are for the frequencies 195, 295, 395 Hz, and the thick line is the Bartlett power averaged over all three frequencies.

power from the MF inversion is defined as

$$P_{\mathrm{BT,\ max}} = \max\ \mathrm{EIV}[\widehat{\mathbf{R}}], \tag{2.2}$$

where EIV denotes the eigenvalues of the matrix. Due to noise contamination in the data, the value of $P_{\mathrm{BT,\ max}}$ must be less than one. In the following analysis, we shall use this value as a measure of SNR.

Under the assumption of statistical stationarity, each value of CSDM was estimated from 4 snapshots which span a time interval of 32 sec and cover about 48 m in source range. Figure 2.6 shows $P_{\mathrm{BT,\ max}}$ as a function of time on a linear scale for each single frequency 195, 295, and 395 Hz (thin lines), as well as for all three frequencies (thick line) for which the power is defined as the average of $P_{\mathrm{BT,\ max}}$ over the three frequencies. During the first 10 minutes of the acoustic transmissions, the ship was stationary and high values of $P_{\mathrm{BT,\ max}}$ are seen in the figure. As the ship began to move away from the VLA, the SNR decreased resulting in the values of $P_{\mathrm{BT,\ max}}$ being lower.

2.4 Matched-Field Geoacoustic Inversion

In this section, the procedure and the required components for the MF geoacoustic inversion are addressed. To prepare for the inversion, an acoustic propagation model and a parameterized environmental model must be chosen. An appropriate objective function and an optimization algorithm must also be defined or selected. The sensitivity of the objective function with respect to environmental variability needs to be tested and the quality of the inversion should be measured.

2.4.1 Acoustic Propagation Model

For ranges greater than several water depths, the acoustic pressure field may be expressed as a finite sum of normal modes. A general bathymetric and geological survey has indicated that in the neighborhood of the experimental site the environment is nearly range-independent. Therefore, the acoustic pressure at a depth z and range r produced by a time-harmonic $\mathrm{e}^{-i\omega t}$ point source at depth z_s in an environment with arbitrary sound speed distribution may be expressed as [53]

$$p(r,z) = \frac{i\mathrm{e}^{-i\pi/4}}{\rho(z_s)\sqrt{8\pi r}} \sum_{n=1}^{N} \Psi_n(z_s)\Psi_n(z)\frac{\mathrm{e}^{ik_{rn}r}}{\sqrt{k_{rn}}} \tag{2.3}$$

where Ψ_n is the n-th normal mode corresponding to the horizontal wavenumber, k_{rn}. The calculations of the modeled acoustic pressure fields were performed by the SACLANTCEN Normal-mode Acoustic Propagation program (SNAP) [52].

2.4.2 Environmental and Array Parameterizations

As mentioned previously, the experimental area is characterized by a fairly flat bottom. The environment is modeled as a waveguide with a constant water depth over a two-layered seafloor as shown schematically in Fig. 2.7. The water depth is known to be approximately 105.5 m. The seafloor is modeled as a uniform sediment layer with sound speed c_{sed}, density ρ_{sed}, attenuation α_{sed}, and thickness d, overlying a semi-infinite subbottom. The sound speeds in these two layers are related by

$$c_{\text{sub}} = c_{\text{sed}} + \Delta c \tag{2.4}$$

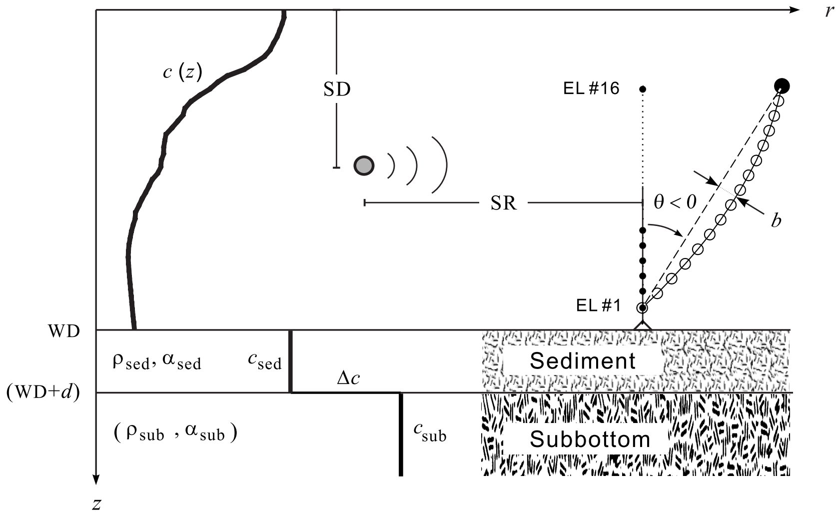

Figure 2.7: Geoacoustic model and experimental configuration for the ASIAEX 2001 East China Sea experiment. Thick lines indicate schematically the sound speed distribution in the water and in the bottom. For the nomenclature, see Table 2.2.

where Δc is the sound speed difference between the two layers and is a positive value. The above-mentioned unknown parameters are estimated in the inversion along with the water depth (although it is known from direct measurement). As for the density and attenuation of the subbottom, separate simulations suggest that the inversion result is relatively insensitive to these parameter values. Therefore, rather than inverting for them, they were set at nominal values of density 2.4 g/cm^3 and attenuation 0.01 dB/λ.

For optimal array-processing, it is necessary to determine the relative positions of the sensors. To achieve a loss of less than 1 dB in conventional array-processing gain requires that the element positions be prior known within a distance of $\lambda/10$, where λ is the wavelength at the frequency of interest [43]. Due to the effects of a nonuniformly-distributed tidal current over the water column as indicated in Section 2.2.2, the VLA might be tilted and curved. To account for the array curvature, a parabolic VLA shape is assumed and the geometry of the VLA is specified in terms of the bow b at the mid-point of the array as shown in Fig. 2.7 and the length of the undisturbed straight array L_s. Note that the value of L_s is known and equals 75 m. According to this geometry, the location of each array element (assuming $\theta = 0$) becomes

$$(x_\mathrm{p}, z_\mathrm{p}) = \left(\frac{4b}{L_\mathrm{s}^2} (L_\mathrm{s} - z_\mathrm{s})\, z_\mathrm{s}, \;\; \left(1 - \frac{8}{3}\frac{b^2}{L_\mathrm{s}^2}\right) z_\mathrm{s} \right) \tag{2.5}$$

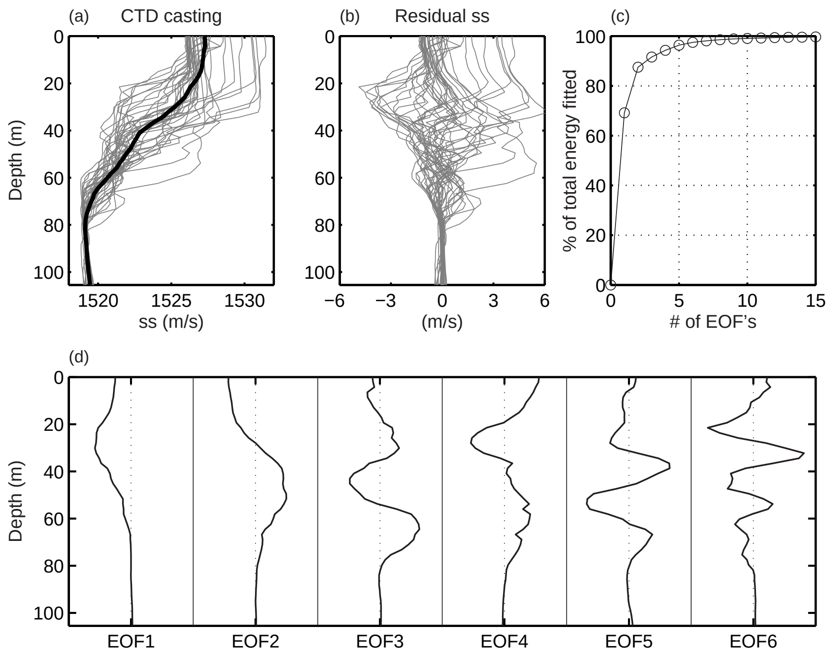

Figure 2.8: Empirical Orthogonal Function (EOF) analysis for the 2001 ASIAEX CTD casts. (a) sound-speed profiles measured from R/V *Melville* and the average sound-speed profile (thick black line); (b) Residual sound-speed profiles; (c) Percent of total fit energy with limited sets of EOF's; (d) First 6 EOF's.

where the subscripts s and p denote the straight and the parabolic arrays, respectively. Then, the tilt of the array is determined by the angle θ. A negative value of θ indicates the array is tilting away from the source. (A 1° tilt corresponds to a approximately 1.3-m horizontal displacement at the topmost array element.)

Because the sound speed difference in the thermocline layer was significant between CTD0123 and CTD0547, an Empirical Orthogonal Function (EOF) analysis of the sound speed measurements [58] was carried out. Figure 2.8 summarizes the EOF analysis for the sound-speed profile measurements. Figure 2.8(a) shows the ensemble of CTD casts from JD 149 to 162 and the average sound-speed profile (thick line); Fig. 2.8(b) shows the variations of residual sound-speed profiles; Fig. 2.8(c) shows the percent of total fit energy, i.e., eigenvalues, within the first 15 EOF's; the shape of the first 6 empirical orthogonal functions is shown in Fig. 2.8(d). It shows that the first 4 EOF's contain about 95 % of the energy.

Table 2.1: The EOF Coefficients for the Measured Sound-Speed Profiles Listed on Fig. 2.4.

Measured SSP	EOF 1	EOF 2	EOF 3	EOF 4	EOF 5	EOF 6
CTD0123	9.39	−0.63	−0.80	1.97	2.20	−0.27
CTD0547	6.77	−2.50	0.52	2.79	0.03	−0.28
CTD0820	11.95	−4.04	−2.73	1.45	0.21	0.68

EOF i denotes the i-th EOF coefficient.

Table 2.1 shows the EOF coefficients for three CTD's taken on JD 158. The search bounds in the estimate of the ocean sound-speed profile are based on this table. The ocean sound-speed profile is modeled by the first three EOF's with CTD0547 as the baseline model.

The forward model parameters can be divided into three subsets: geometrical, geoacoustic and ocean sound speed parameters. Table 2.2 lists each inversion parameter along with their search bounds. These values were selected based upon *a priori* knowledge about the environment.

2.4.3 Objective Function

The objective function measures the discrepancy between the measured acoustic field and replica fields calculated for likely values of the unknown parameters. The data misfit objective function chosen here is based on the incoherent multi-frequency Bartlett processor [63]. Under the assumption of no spatial coherence across frequencies, the misfit objective function can be expressed as

$$\begin{aligned} \phi(\mathbf{m}) &= \frac{1}{L}\sum_{l=1}^{L}\left[1-\mathbf{d}_l^{\dagger}(\mathbf{m})\widehat{\mathbf{R}}_l\mathbf{d}_l(\mathbf{m})\right] && (2.6) \\ &= 1-\frac{1}{L}\sum_{l=1}^{L}P_{\mathrm{BT},l}(\mathbf{m}) && (2.7) \end{aligned}$$

where $\mathbf{d}(\mathbf{m})$ is the replica field generated for the vector of unknown parameters $\mathbf{m}$, normalized to have unit length, $\widehat{\mathbf{R}}$ is an estimated CSDM as given in Eq. (2.1), and L is the number of source frequencies. The misfit objective function can be re-written

Table 2.2: Inversion Parameters with Search Bounds

Model parameter		Search bounds	
Description	Symbol	Lower	Upper
Geometrical			
Source range (m)	SR	1650	1800
Source depth (m)	SD	46	51
Water depth (m)	WD	104	108
Bow of parabola (m)	b	0.5	2
Array tilt (deg)	θ	-7	-5
Geoacoustic			
Sediment			
Comp. speed (m/s)	c_{sed}	1550	1650
Attenuation (dB/λ)	α_{sed}	0.01	0.5
Density (g/cm^3)	ρ_{sed}	1.3	2.2
Subbottom			
Increase comp. speed (m/s)	Δc	10	200
Depth of subbottom (m)	d	1	20
Ocean sound speed			
EOF 1		5	10
EOF 2		-5	0
EOF 3		-3	3

The search interval for each parameter was discretized into 128 points.
The array tilt refers to the angle with respect to the vertical axis.
(negative in the direction away from the source).

as a function of the Bartlett power as shown in Eq. (2.7), in which the second term is the arithmetic mean of Bartlett powers over the selected frequencies. By minimizing the misfit objective function, the most likely values of the environmental parameters can be found.

2.4.4 Sensitivity Analysis

To investigate the relative importance of the parameters, a sensitivity study was carried out. Figure 2.9 summarizes the sound-field sensitivity for the selected frequencies 195, 295, and 395 Hz for the model parameters given in Table 2.2. The sensitivity of the Bartlett power for the given frequency and the given parameter was computed by correlating the data vector generated by the "true" parameter value with replica vectors computed by varying the parameter value. In each case, the parameters that are not varied are held at their nominal values (the values taken from the best-fit model at T = 29 min) and the search bounds of each parameter were as shown in Table 2.2. A sensitivity index (SI) for a particular parameter m_i is obtained by incorporating the minimum point in the sensitivity curve, $P_{\mathrm{BT}}(m_i')/P_{\mathrm{BT}}(m_i)$, in the following expression:

$$\mathrm{SI}\ (m_i) = 1 - \min_{l_i \leq m_i' \leq u_i} P_{\mathrm{BT}}(m_i')/P_{\mathrm{BT}}(m_i) \tag{2.8}$$

where m_i' denotes the values taken from the search interval between the lower bound l_i and the upper bound u_i. $P_{\mathrm{BT}}(m_i)$ is always one due to no noise in the simulation. For highly sensitive parameters, SI is almost one which means that the correlation degrades rapidly as the parameter value departs from the "true" value. For less sensitive or the so-called non-identifiable parameters, the correlation remains about the same even with some changes in such parameters. Note that the value of SI for each parameter is also dependent on the corresponding search bounds. However, this measure of sensitivity is useful for inter-frequency comparison.

2.4.5 Genetic Algorithms

Genetic algorithms (GA's) are robust search mechanisms based on underlying genetic biological principles. The complete description is well documented in [34]. The values of the GA parameters used in this analysis are as follows: the population size was

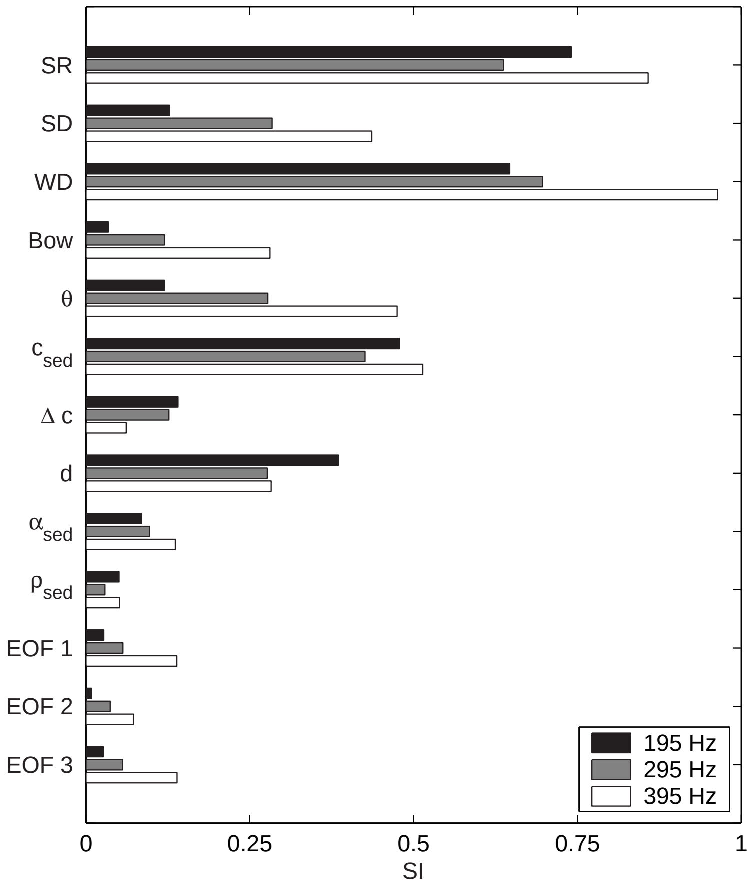

Figure 2.9: The sensitivity index for the model parameters given in Table 2.2 .

set to 64, reproduction size was 0.5, crossover probability was 0.8, mutation probability was 0.05, and number of forward model computations for each population was 2500. However, to collect statistical information in order to estimate the parameter uncertainty, the number of parallel populations was set to 45. Approximately 112,500 forward models were run.

2.4.6 Uncertainty Estimates

Because of the ambiguity imposed by data incompleteness, measurement noise, and theoretical simplifications of the environment, a range of model parameters may explain the data equally well. The global optimization method in SAGA is used to obtain the samples of the search space. To estimate the parameter uncertainty, the obtained samples are then used to calculate the posterior probability density (PPD) as follows [76]:

$$P(\mathbf{m}) = \frac{\mathcal{L}(\mathbf{m})}{\sum_{j=1}^{N_{\text{obs}}} \mathcal{L}(\mathbf{m}^j)} \tag{2.9}$$

where N_{obs} is the total number of observations (forward model runs). Under the assumption of Gaussian errors, the likelihood function $\mathcal{L}(\mathbf{m})$ is related to the objective function $\phi(\mathbf{m})$ through an exponential $\mathcal{L}(\mathbf{m}) \propto \exp(-\phi(\mathbf{m}))$. From the PPD, the mean model parameter $\langle \mathbf{m} \rangle$ and the model covariance matrix $\text{Cov}(\mathbf{m})$ can be estimated, respectively, as follows:

$$\langle \mathbf{m} \rangle = \sum \mathbf{m} P(\mathbf{m}) \tag{2.10}$$

$$\text{Cov}(\mathbf{m}) = \sum \mathbf{m}\mathbf{m}^{\text{T}} P(\mathbf{m}) - \langle \mathbf{m} \rangle \langle \mathbf{m} \rangle^{\text{T}} \tag{2.11}$$

where T denotes the transpose operation, and the sum is taken over the total observations. A measure of the accuracy of the inversion is defined as standard deviations of the model parameters computed by the square roots of the diagonal terms of $\text{Cov}(\mathbf{m})$.

2.5 Results and Discussion

Matched-field geoacoustic inversion using the selected frequencies 195, 295, and 395 Hz was carried out at T = 29 min over a parameter space of 13 parameters including the geometrical, geoacoustic, and ocean sound speed EOF coefficients. Based upon the GPS measurement on R/V *Melville*, the source was approximately 1.7 km away from the VLA. Figure 2.10 shows the marginal dot diagrams for the model parameters. The vertical axis is the achieved misfit (i.e., Eq. (2.7)) with respect to the parameter sampled during the SAGA optimization. The thick line superimposed on each scatter plot was obtained by using the best-fit model corresponding to the optimal value of the objective function as a baseline and computing the sensitivity for the optimized parameter. We see that the sampled values for the array bow and tilt parameters (b and θ) are spread mainly inside the sensitivity curve and align mostly with the best-fit values. A similar behavior is observed for the ocean sound speed EOF coefficients but with a wider span. The consistency between the local (line) and global (dots) searches shows that this set of parameters is weakly correlated with the other parameters. For the geoacoustic parameters, most sampled values wander outside the curve. This reveals the more complicated structure in the multi-dimensional search space. Note that the sampled values for the source range (SR) and the water depth (WD) are spread uniformly throughout the range of the parameter interval. This is due to the strong coupling between these two parameters.

Parameter coupling is another factor that determines the degree of uncertainty in the model parameter estimates. Figure 2.11 shows the two-dimensional cross-sections of Bartlett power for the selected parameters. The colorbar next to each plot indicates the dynamic range in terms of dB. The two-dimensional dependence of Bartlett power on SR and WD (Fig. 2.11(a)) exhibits a long narrow ridge indicating a strong correlation between these two parameters. Similar correlations between c_{sed} and WD, and c_{sed} and d are illustrated in Figs. 2.11(c) and (d), respectively. In each case, similar Bartlett power would be achieved with increases in both parameters. As a result, high values of one parameter tend to occur consistently with high values of the other parameter during the SAGA optimization. Physically, the positive correlation between the water depth (WD) and the source range (SR) can be explained by the waveguide invariant [26].

The SAGA-determined best-fit parameters and the mean estimated from the PPD along with their standard deviations are tabulated in Table 2.3. Note that $\text{SAGA}_{\text{best}}$ and $\text{SAGA}_{\text{mean}}$ estimated model parameters are not necessarily equal. This is due to the nonlinear relation between the data and the model parameters, a data set with a

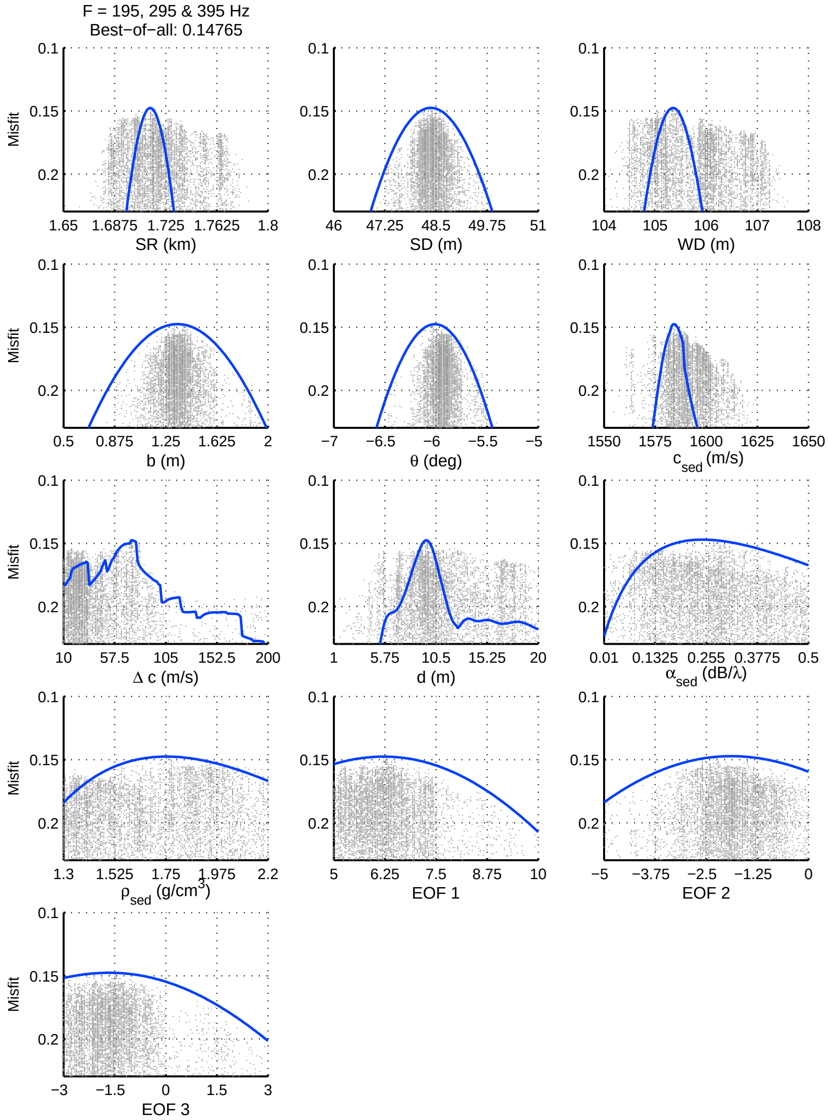

Figure 2.10: Marginal dot diagrams of the SAGA search for the model parameters. The vertical axis represents the attained misfit on a linear scale. The thick line is the sensitivity curve of the multi-frequency misfit function using the best-fit model as a baseline.

Table 2.3: Parameter Estimates at SR = 1.7 km

Parameter		$\text{SAGA}_{\text{best}}$	$\text{SAGA}_{\text{mean}} \pm \sigma$
SR	(m)	1714	1714 ± 16
SD	(m)	48.3	48.4 ± 0.2
WD	(m)	105.4	105.4 ± 0.6
b	(m)	1.3	1.3 ± 0.1
θ	(deg)	-6.02	-6.02 ± 0.08
c_{sed}	(m/s)	1585	1588 ± 7
Δc	(m/s)	74	43 ± 24
d	(m)	10	10 ± 3
α_{sed}	(dB/λ)	0.28	0.2 ± 0.1
ρ_{sed}	(g/cm^3)	1.8	1.8 ± 0.2
EOF 1		6.3	6.1 ± 0.6
EOF 2		-2.2	-2.0 ± 0.6
EOF 3		-1.6	-1.7 ± 0.7

σ indicates the standard deviation.

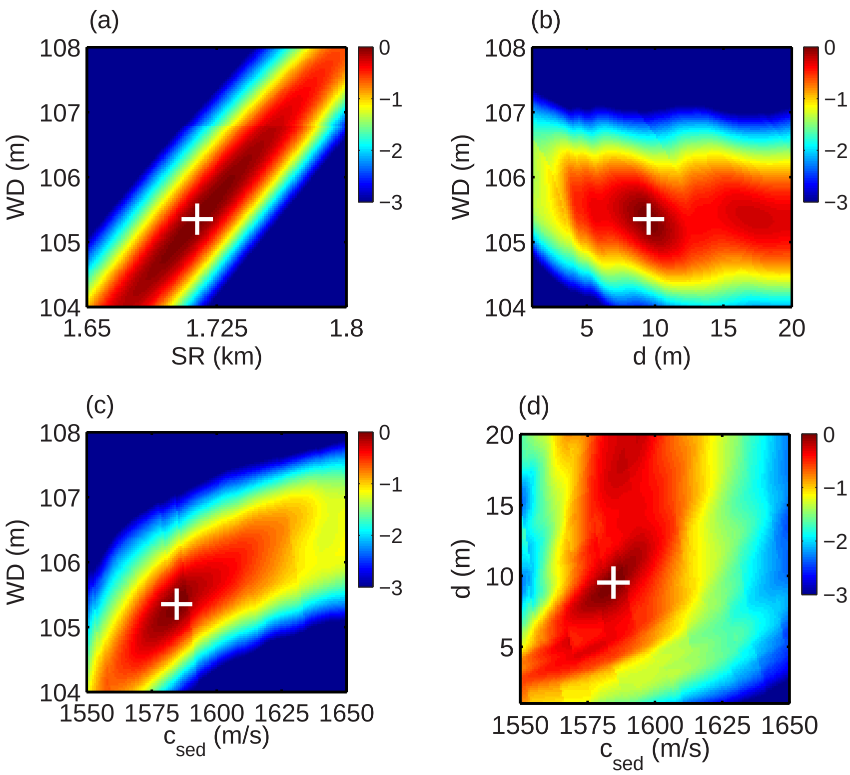

Figure 2.11: Two-dimensional cross-sections of Bartlett power for the selected model parameter estimated at SR = 1.7 km. The plus signs indicate the true parameter values taken from the SAGA best-fit model. (synthetic cases)

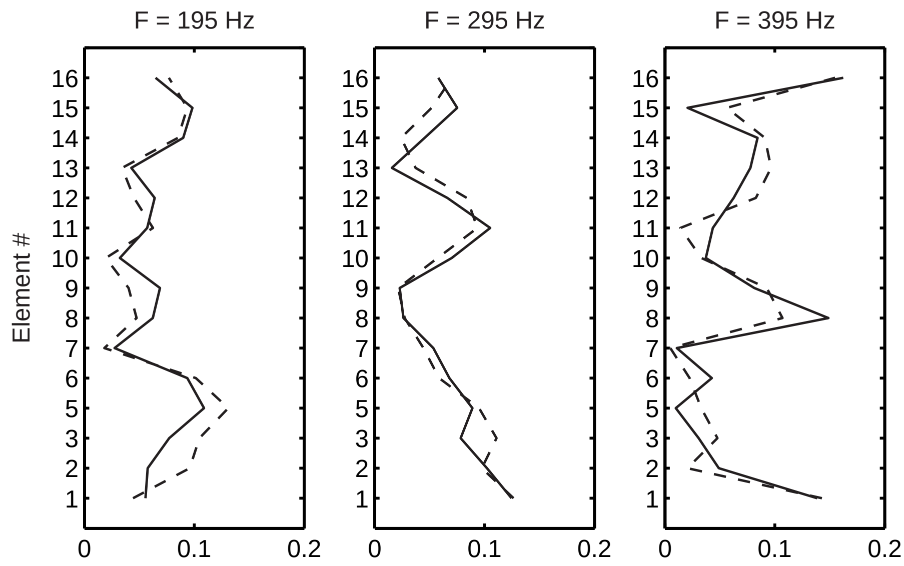

Figure 2.12: Comparison of the observed and modeled fields on the vertical array for each of the frequencies used in the inversion. The solid and dashed lines indicate the magnitude of the observed and modeled fields, respectively. Note that element #4 has been deleted.

Gaussian error law in general is mapped onto a estimator of the model having a non-symmetric density function.

It shows that the geometrical parameters (SR, SD, WD, b, θ), sediment sound speed (c_{sed}), and the sediment thickness (d) all are well-determined. However, the parameter Δc isn't well-determined (the SAGA best-fit value is outside the mean plus one standard deviation). Although the sediment attenuation and density have low sensitivity, the standard deviation also is relatively small due to the narrow search bounds selected for these two parameters.

Figure 2.12 shows the comparison of the observed and modeled fields on the vertical array for each of the frequencies used in the inversion. The solid line represents the magnitude of the observed field normalized by the total power registered at VLA and the dashed line represents the magnitude of the modeled field computed by the best-fit model and similarly normalized. The comparison shows good agreement between the observed and modeled data for the frequencies 195, 295, and 395 Hz.

2.5.1 Source Localizations

The inversion quality also is checked by using MF processing for source localization. The replica pressure field computed by the best-fit model from the inversion carried out at SR = 1.7 km was used in this subsection. To avoid search grid mismatch in the frequency band of interest [56], the grid spacings Δr and Δz were set to be 10 m and 1 m, respectively. Figure 2.13 shows the source range-depth ambiguity surfaces for each source frequency and the multi-frequency average at SR = 1.7 km. The multi-frequency ambiguity surface is defined as the arithmetic mean of MF correlations over the selected frequencies. We see the distinguishing mainlobe/sidelobe structure and the high MF correlations for both single and multiple frequencies.

An environmental model that localizes the source at one range may not localize the source at another range. In order to confirm the applicability of the environmental model estimated at SR = 1.7 km, this model was also applied to the data from a greater range. Figure 2.14 shows the ambiguity surface at T = 42 min using the environmental parameters listed in Table 2.3. The grid spacing $(\Delta r, \Delta z)$ was the same as before. The results in Fig. 2.14 show that the peak on each ambiguity surface still remains at a high correlation level and the peak locations for the different frequencies are located at the same range/depth and agree with the experimental configuration.

Encouraged by the consistency of the geoacoustic model at two different ranges, we then applied this model on the acoustic data over the time interval from 20 to 50 minutes. First, an exhaustive search was conducted over three of the geometrical parameters (SR, SD and θ) at 295 Hz. Figure 2.15 shows the MF correlations over time for different array tilts. As mentioned in Section 2.4.2, the accuracy to which sensor positions should be known has to be better than $\lambda/10$. *A priori* information showed that the array was not purely vertical and it had some tilt on the order of -5 or -7 degrees from vertical. Due to the current force on the VLA, the source and the VLA are not in the same vertical plane in which the r-axis is defined by the source and the deepest array element. Therefore, from the perspective of the source, the apparent tilt of the array changes over time. In Fig. 2.15, the bow of the array was taken to be the estimated value from the inversion and θ varies from -5 to -7 degrees in 0.5 degree increments. The tilt is such that the uppermost part of the array is farther away from the source than the

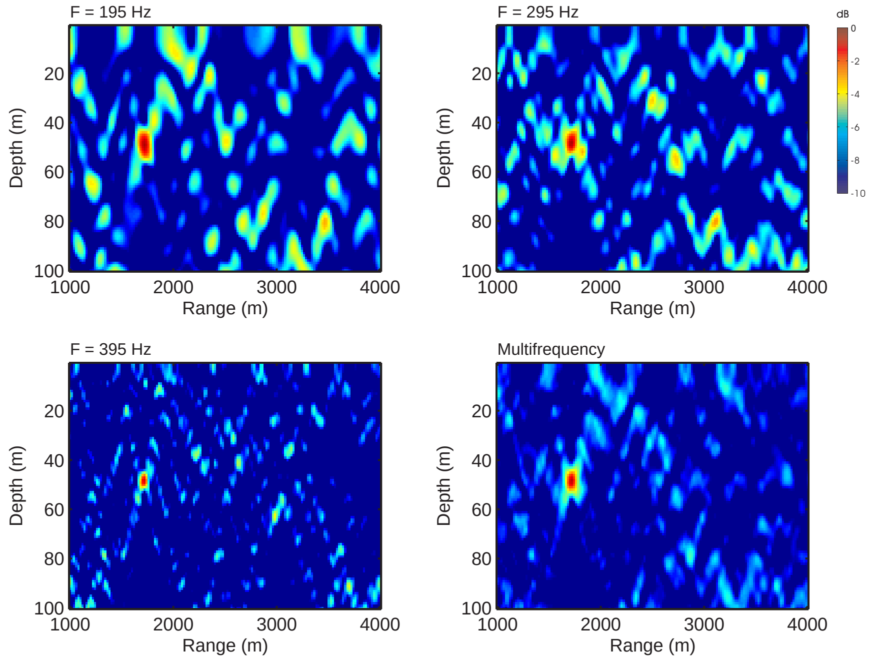

Figure 2.13: Range-depth ambiguity surfaces at SR = 1.7 km. The replica pressure field is computed using the environmental parameters listed in Table 2.3.

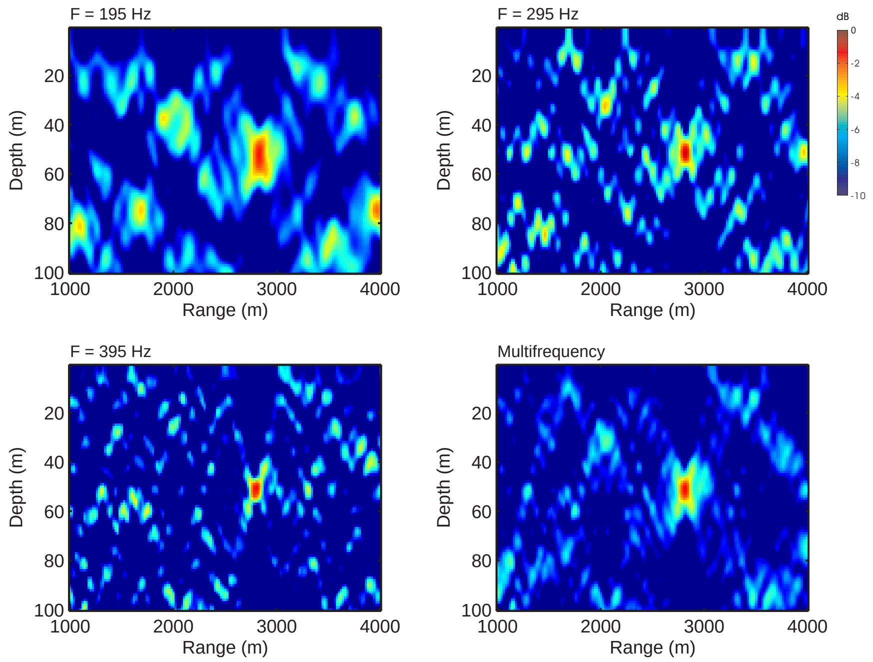

Figure 2.14: Range-depth ambiguity surfaces at SR = 2.8 km. The replica field is computed using the environmental parameters listed in Table 2.3.

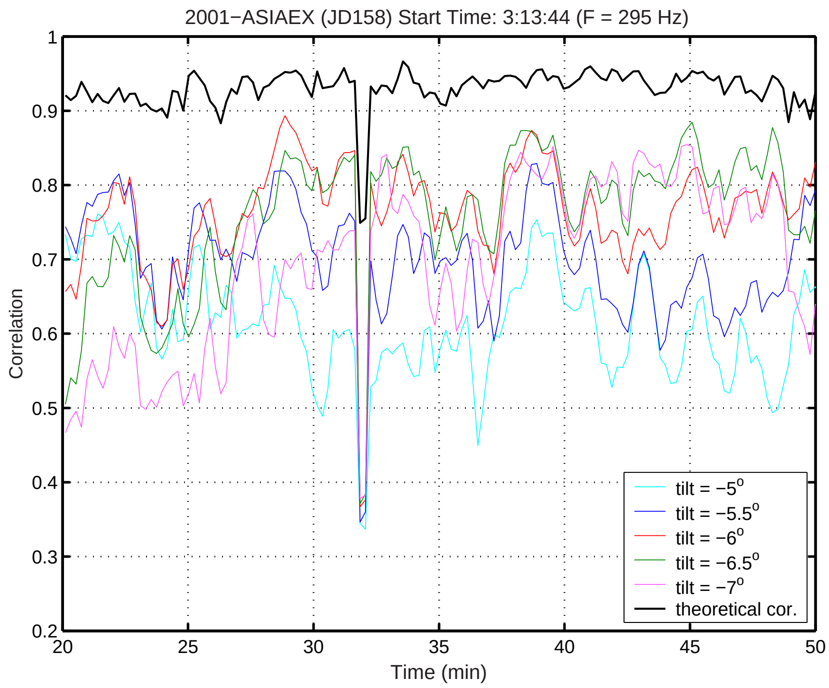

Figure 2.15: MF correlations over time for different array tilts at 295 Hz. The replica pressure field is computed using the environmental parameters listed in Table 2.3.

lower part of the array. As expected, the highest MF correlation appears at the range where the inversion was carried out.

MF-derived source-receiver range and source depth using 195, 295, and 395 Hz over the time interval from 20 to 50 minutes are displayed in Figs. 2.16 and 2.17, respectively. The peak tilt correlations shown in Fig. 2.15 were used as a guide for which tilts to use in this time period. Based upon the GPS measurements, the data in this time interval cover the range from 1 to 3.5 km. The source depths measured by the depth sensor are indicated by the plus signs in Fig. 2.17. Compared with the GPS and the depth sensor measurements, MF-derived source position is consistent with the experimental configuration. Source localization based on the best-fit model tracks the actual source positions well.

2.5.2 Inversion Results over Time

As a final example, separate inversions were carried out using the acoustic data at each range over the time interval from 20 to 40 minutes. The GA parameters and the

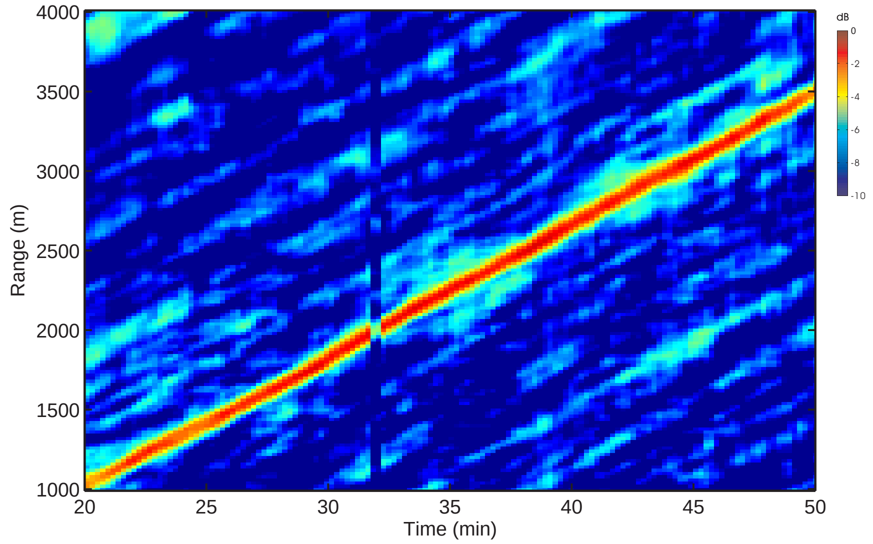

Figure 2.16: MF-derived source-receiver range over the time interval from 20 to 50 min.

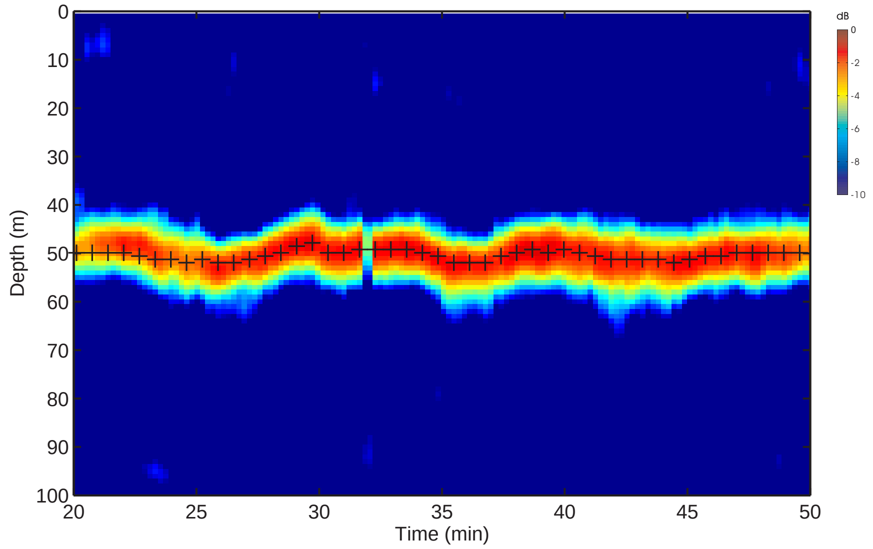

Figure 2.17: MF-derived source depth over the same time interval shown in Fig. 2.16. The plus signs indicate the true measured values.

search bounds were taken to be the same as the inversion conducted at T = 29 min except for SR. Approximately 10^7 forward models were computed for a total of 98 inversions.

The purpose of inverting the data at many ranges is to consider a large enough number of separate measurements to provide an indication of the consistency of the inversion results for the various model parameters. Figure 2.18 shows the lowest misfit objective function and the corresponding model parameters (best-fit model) determined in all inversions plotted as a function of time.

The best-fit model at each range was obtained by minimizing the misfit objective function ϕ between measured and modeled fields. The lowest misfits obtained by the SAGA inversions (the cross signs connected by a solid line) are shown in Fig. 2.18(a). The solid line represents the best possible value of misfit for the available SNR (i.e., $1 - P_{\mathrm{BT,\,max}}$, see Eq. (2.2)). We see that low misfit values were obtained for all ranges. The best-fit results for SR and SD (Figs. 2.18(b) and (c), respectively) closely track the source position. The estimated water depth (Fig. 2.18(d)) exhibits the mild variation from inversion to inversion. The estimated array bow (Fig. 2.18(e)) shows a small amount of variation. The reason is that the current essentially was constant in direction and magnitude over this 20-minute time interval. The inversion results for the array tilt shown in Fig. 2.18(f) are in good agreement with the tilts determined by searching over only three geometrical parameters: SR, SD, and θ using 295 Hz (Fig. 2.15). Figures 2.18(g)–(k) show the inversion results for the geoacoustic parameters: sediment sound speeds c_{sed}, Δc, and sediment thickness d, attenuation α_{sed}, and density ρ_{sed}. Consistent values were obtained for geometrical parameters and sediment sound speed, attenuation, and thickness. Figures 2.18(l)–(n) show the inversion results for the first three ocean sound speed EOF coefficients

The parameter uncertainty was estimated using the best-fit models determined at each range over the time interval from 20 to 40 minutes. The mean and standard deviation for each of the parameters is indicated by the solid and dashed lines, respectively. Compared with the SAGA parameter estimate at SR = 1.7 km, the mean and standard deviation for each of the parameters is in excellent agreement. Table 2.4 summarizes the results of the comparison.

Since separate inversions were carried out for the acoustic data at each range

Table 2.4: Comparison of the Parameter Uncertainty Estimates

Parameter	Multiple Range Inversions	Single Range Inversion	
	Mean $\pm$ STD	$\text{SAGA}_{\text{mean}} \pm \sigma$	$\text{SAGA}_{\text{best}}$
c_{sed} (m/s)	1582 ± 9	1588 ± 7	1585
Δc (m/s)	55 ± 32	43 ± 24	74
d (m)	11 ± 3	10 ± 3	10
α_{sed} (dB/λ)	0.2 ± 0.1	0.2 ± 0.1	0.28
ρ_{sed} (g/cm^3)	1.9 ± 0.2	1.8 ± 0.2	1.8
EOF 1	6.4 ± 1.1	6.1 ± 0.6	6.3
EOF 2	-2.2 ± 0.8	-2.0 ± 0.6	-2.2
EOF 3	-0.7 ± 0.9	-1.7 ± 0.7	-1.6

Multiple Range Inversions: the means and standard deviations (STD) of the inversion results of Fig. 2.18.

Single Range Inversion: the best-fit model, and the PPD mean and standard deviation estimated at SR = 1.7 km.

over the 20-minute duration, a comparison of the measured and modeled acoustic fields at selected array elements was made. Figure 2.19 demonstrates the agreement between the observed and modeled fields. The measured field (solid line) was normalized by the total power registered at VLA at each range and the modeled field (dashed line) was computed using the best-fit model at each range and similarly normalized. It shows that the model fields reproduce the major features of the measured field reasonably well.

The variation from inversion to inversion in each parameter is used to examine parameter coupling. The coupling between model parameters can be quantified using the correlation coefficient matrix $\boldsymbol{\rho}$, defined by

$$\rho_{ij} = \frac{C_{M_{ij}}}{\sqrt{C_{M_{ii}} C_{M_{jj}}}} \tag{2.12}$$

where the covariance matrix $\mathbf{C_M}$ is calculated by

$$\mathbf{C_M} = \langle (\mathbf{m}_{\text{best}} - \langle \mathbf{m}_{\text{best}} \rangle)(\mathbf{m}_{\text{best}} - \langle \mathbf{m}_{\text{best}} \rangle)^T \rangle \tag{2.13}$$

with $\mathbf{m}_{\text{best}}$ is the best-fit model found at each inversion. Values of ρ_{ij} are bounded between -1 and $+1$, with $-1(+1)$ indicating a perfect negative (positive) correlation between parameters i and j, and 0 indicating uncorrelated parameters. For the purpose of demonstrating parameter coupling, only the absolute value of the correlation coefficient is considered. Figure 2.20 presents the magnitude of the linear correlation coefficient computed using the inversion results shown in Fig. 2.18. A strong coupling was observed for the following parameter pairs (WD, d), (WD, c_{sed}), and (d, c_{sed}), which is consistent with the observations in Fig. 2.11.

2.6 Conclusions

This chapter reports the geoacoustic inversion results based upon source tow data obtained during the ASIAEX 2001 East China Sea experiment. The source tow data recorded on a VLA were used to estimate the geoacoustic properties of the seafloor. The waveguide was assumed to be range-independent, and the seafloor was modeled as a homogeneous sediment layer overlying a semi-infinite subbottom.

Matched-field geoacoustic inversions using frequencies 195, 295, and 395 Hz were carried out by a genetic-algorithm-based optimization approach. The environmental

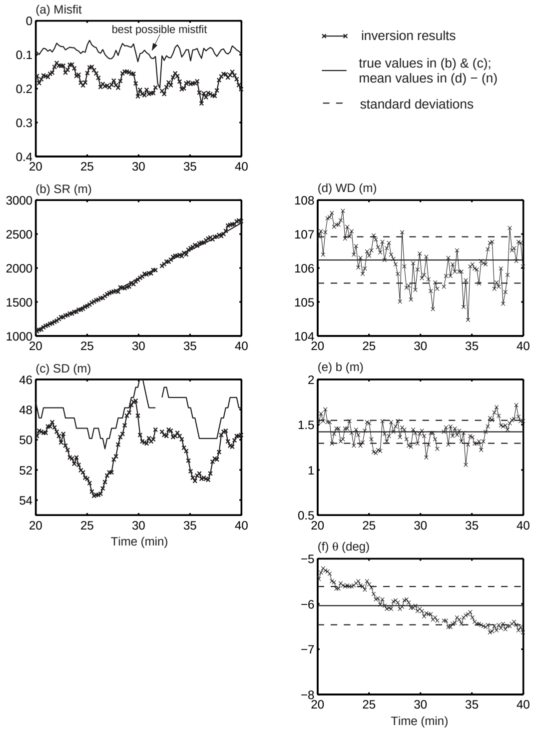

Figure 2.18: The inverted environmental parameter values versus time. (a) the solid line shows the best possible value for the available SNR and the cross signs connected by a solid line represents the lowest misfit attained by SAGA. (b)–(f) show the results for the geometrical parameters. The solid lines in (b) and (c) indicate the true measured values.

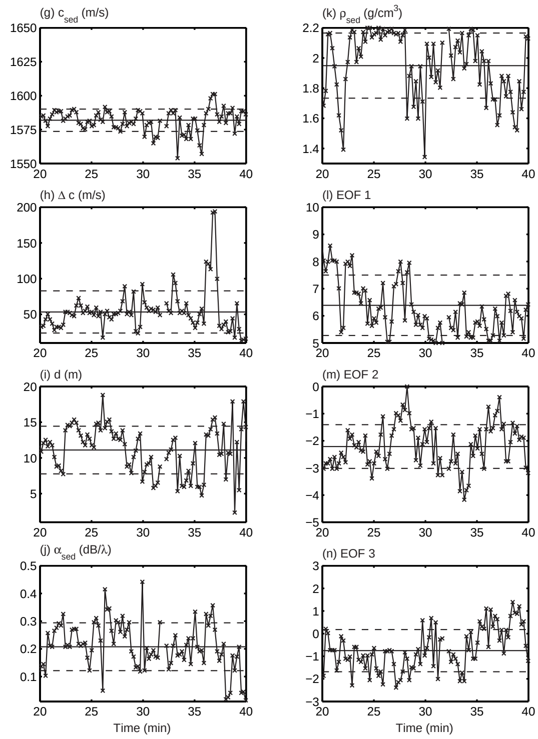

Figure 2.18: (cont'd) (g)–(k) show the results for the geoacoustic parameters; (l)–(n) show the results for the ocean sound speed EOF coefficients. The crosses connected by a solid line indicate the SAGA best-fit results. The solid and dashed lines indicate the mean and plus/minus one standard deviation of the mean, respectively. The vertical axis represents the search bounds.

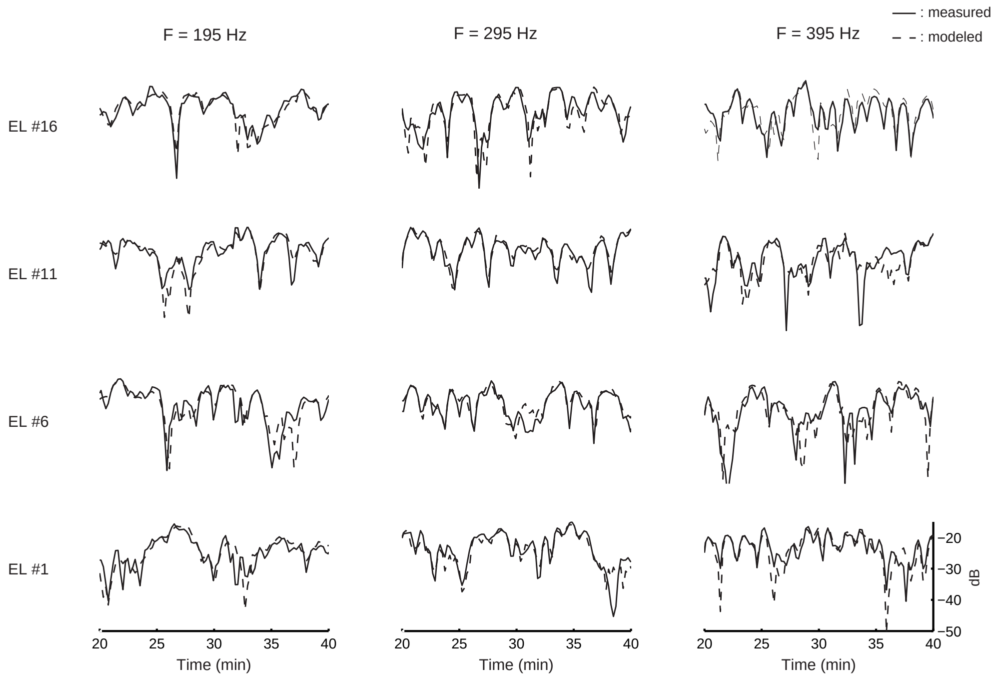

Figure 2.19: Normalized received levels for the measured (solid line) and normalized modeled (dashed line) fields as a function of time for the array elements 1, 6, 11, and 16 and for the frequencies 195, 295, and 395 Hz. The modeled fields were computed using the best-fit model found at each range.

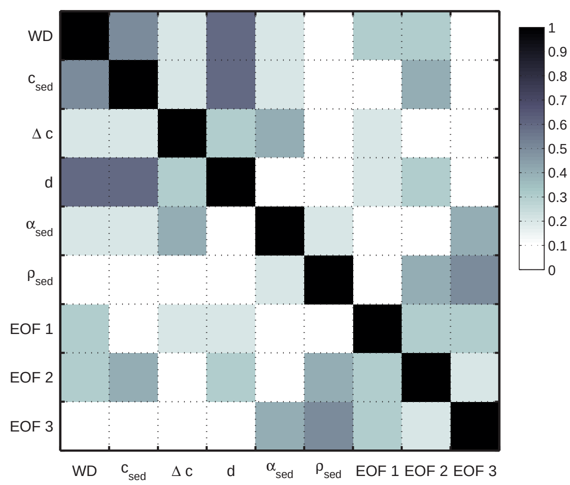

Figure 2.20: Correlation coefficient matrix for the environmental parameters computed using the inversion results shown in Fig. 2.18.

parameters were estimated by two different analyses to ensure the robustness of the inversion. These two analyses are summarized as follows:

1. The inversion was first performed with the set of data obtained at range of SR = 1.7 km. The accuracy of the inverted parameters was measured by the mean and the standard deviation of the posterior probability distribution. The results indicated a good agreement between the measured and the modeled sound fields. Furthermore, the inverted model quality was checked by using MF processing for source localization over the entire 30-min time interval. The predicted source positions track the measurements well.
2. A total of 98 separate inversions were carried out for the acoustic data at each range over the time interval from 20 to 40 minutes. The best-fit model at each range is the inversion result at that range. The data in this time interval covers a 1.5-km range. With the assumption that the seabed properties are range-independent, the resulting variations from inversion to inversion were used to analyze the parameter uncertainty. Low misfit values were obtained for all ranges, and consistent values were obtained for geometrical parameters and sediment sound speed, attenuation, and thickness. Also, a comparison of the measured and modeled fields was made and shows good agreement.

The parameter uncertainty (the mean and standard deviation) estimated from several inversions are in excellent agreement with the results at SR = 1.7 km. Parameter coupling was examined using the correlation coefficient matrix derived from the multi-range inversion results. The observed parameter correlations were consistent with our sensitivity results at SR = 1.7 km.

This chapter in part is a reprint of the material as it appears in Chen-Fen Huang and William S. Hodgkiss, "Matched field geoacoustic inversion of low frequency source tow data from the ASIAEX East China Sea experiment," IEEE J. Oceanic Eng., Vol. 29, 952–963, 2004. The dissertation author was the primary researcher/author and the co-author listed in this publication directed and supervised the research which forms the basis for this chapter.